

# Effects of Stress and Electromigration on Microstructural Evolution in Microbumps of Three-Dimensional Integrated Circuits

Hua Xiong, Zhiheng Huang, *Member, IEEE*, and Paul Conway, *Senior Member, IEEE*

**Abstract**—Due to geometric scaling, the heterogeneous and anisotropic microstructures present in through-silicon vias and microbumps must be considered in the stress management of 3D integrated circuits. In this study, a phase-field model is developed to investigate the effects of stress and electromigration on microstructural evolution in a Cu/Sn-microbump/Cu structure at 150°C. External compressive stress is observed to accelerate the growth of Cu<sub>3</sub>Sn grains and cause the separation of continuous interfacial Cu<sub>6</sub>Sn<sub>5</sub> grains by β-Sn grains, while tensile stress promotes the growth of Cu<sub>6</sub>Sn<sub>5</sub> grains and the formation of a continuous Cu<sub>6</sub>Sn<sub>5</sub> layer. The roughness of the β-Sn-Cu<sub>6</sub>Sn<sub>5</sub> interface under compressive stress is greater than that under tensile stress. The morphological evolution of the β-Sn grains is also affected by stress. An external shear or compressive stress favors the growth of β-Sn grains with their *c*-axis particular to the *Y* direction. Furthermore, the interdiffusion flux driven by electromigration increases the roughness of the interfacial Cu<sub>6</sub>Sn<sub>5</sub> grains at the cathode. The strain caused by electromigration results in larger β-Sn grains, enabling faster interdiffusion along the current direction. The preferential growth of the β-Sn grains under stress or electromigration decreases the shear modulus of microbumps.

**Index Terms**—Interconnections, tin compounds, modeling, stress, electromigration.

## I. INTRODUCTION

CURRENTLY, a promising solution for enabling higher functional density and heterogeneous integration of circuits is to design devices and packages with a 2.5D or 3D architecture. The management of stresses occurring at multiple scales is a key issue that must be addressed to ensure the high performance and reliability of 3D integrated circuits (ICs) [1]–[5]. At the package level, stresses can cause failures within bumps, cracks within dies, delaminations from dielectric layers, etc. At the chip level, stresses can change the mobility of carriers, i.e., holes and electrons, in devices [6]–[8]. In addition, effects from chip-package interaction (CPI) become stronger in 3D ICs due to the compact integration

Manuscript received August 11, 2014; accepted September 5, 2014. Date of publication , 2014 ; date of current version , 2014.

Hua Xiong is with the School of Physics and Engineering, Sun Yat-sen University, 135 West Xingang Road, Guangzhou 510275, China.

Zhiheng Huang is with the School of Physics and Engineering, Sun Yat-sen University, 135 West Xingang Road, Guangzhou 510275, China (e-mail: hzh29@mail.sysu.edu.cn).

Paul Conway is with the Wolfson School of Mechanical and Manufacturing Engineering, Loughborough University, Loughborough, Leicestershire, LE11 3TU, United Kingdom.

Copyright © 2014 IEEE. Personal use of this material is permitted. However, permission to use this material for any other purposes must be obtained by sending a request to [pubs-permissions@ieee.org](mailto:pubs-permissions@ieee.org)

of chips and interconnects. CPI-induced stress can exacerbate the degradation of materials via processes such as electrical breakdown in inter-metal dielectric, electromigration (EM), and stress migration (SM) [9]. Efficient chip/package co-analysis of mechanical stress has been enabled by lateral and vertical linear superposition (LVSI) methods developed by Jung *et al.* [8]. However, high-fidelity predictions of stress distribution across chips and packages are still restricted by the lack of a database of multi-scale and time-dependent materials properties [1], [10]. In particular, knowledge of microstructure-dependent properties still remains scarce.

In a microbump through-silicon via (TSV) structure, the properties of the microbump are strongly related to the crystallographic orientations of the β-Sn grains and the morphologies of the intermetallic compounds (IMCs) [11], [12]. For example, a microbump as small as a few microns may contain only one or a few grains, which leads to an anisotropic elastic modulus. In addition, the morphology of the IMCs becomes increasingly important because the volume fraction of the IMCs in a microbump will be substantially increased if the temperature and time of the reflow remain at the same level as that in the processing of flip-chip solder joints [11]. In this case, the large number of microbumps in 3D ICs may exhibit non-uniform properties and scatter in reliability performance data.

It is challenging to predict the microstructure within microbumps because the microstructural evolution is influenced by the stresses caused during fabrication and those under subsequent service conditions of the ICs [13]–[16]. For example, Zhou *et al.* observed that the *c*-axis of the β-Sn grains in a Sn3.5Ag solder joint rotated toward a direction parallel to the interface between the solder joint and the under-bump metallization (UBM) due to thermo-mechanical stress [13]. Abdelhadi *et al.* reported faster growth of the Cu<sub>3</sub>Sn IMC in smaller Sn3.5Ag solder joints and attributed this result to the effect of stress on the diffusion rates of Sn and Cu [15]. EM also affects the microstructure within microbumps [17]–[19]. Ke *et al.* reported the formation of a serrated interface between the solder and Cu<sub>6</sub>Sn<sub>5</sub> IMC layer at the cathode due to electromigration [17]. Wu *et al.* observed the rotation of β-Sn grains under current stressing [18]. Although recent studies on stress analyses of 3D ICs have considered static microstructures such as Cu grains drawn artificially [20], [21] or generated by the Voronoi algorithm [22], microstructural evolution has not yet been coupled for analyses carried out

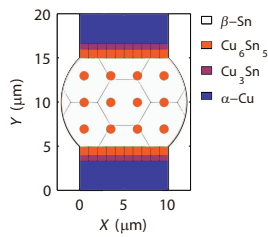


Fig. 1. The geometry and initial microstructure of the Cu/Sn-microbump/Cu structure.

with existing design platforms.

The lack of understanding of the mechanisms underlying stress-driven and EM-driven microstructural evolution is a bottleneck that restricts the accuracy of stress predictions for 3D ICs. Phase-field (PF) models have been used to study microstructural evolution coupled with stress and EM for multiphase materials [23]–[26]. However, no such modeling technique has yet been employed to study microbumps in 3D ICs. On the other hand, PF models of the Sn-Cu binary system have been used to study the mechanisms underlying the morphological evolution of interfacial Cu<sub>6</sub>Sn<sub>5</sub> and Cu<sub>3</sub>Sn IMCs without stress coupling [27]–[30]. The PF models mentioned above are combined and extended in this study to develop a comprehensive PF model to study the effects of stress and EM on microstructural evolution of Cu/Sn-microbump/Cu structures.

## II. MODELING METHODOLOGY

### A. Initial Settings of the Model Structure

The complete set of phases in the Sn-Cu binary system that are thermodynamically stable at 150°C, i.e., β-Sn, Cu<sub>6</sub>Sn<sub>5</sub>, Cu<sub>3</sub>Sn, and α-Cu, are considered in the two-dimensional PF model used in this study. Each of these four phases can be set to consist of multiple grains with different crystallographic orientations. The cross-section of the Cu/Sn-microbump/Cu structure with its initial microstructure is illustrated in Fig. 1. The pad size, standoff height, and initial thicknesses of the interfacial Cu<sub>6</sub>Sn<sub>5</sub> grains, Cu<sub>3</sub>Sn grains, and Cu UBM are set to 10 μm, 20 μm, and 1 μm, 0.6 μm, and 3.4 μm, respectively. The widths of the interfacial Cu<sub>6</sub>Sn<sub>5</sub> and Cu<sub>3</sub>Sn grains in the X direction are set to 1 μm. Bulk Cu<sub>6</sub>Sn<sub>5</sub> particles with a uniform diameter of 1 μm are distributed in a square array in the Sn microbump, as illustrated in Fig. 1, to study the morphologies of the bulk Cu<sub>6</sub>Sn<sub>5</sub> particles at different locations in the microbump. The distance between the two nearest Cu<sub>6</sub>Sn<sub>5</sub> particles is 3 μm, which corresponds to a volume fraction of 8.7% with an assumption that the microbump and the Cu<sub>6</sub>Sn<sub>5</sub> particles are of a truncated sphere and sphere geometries, respectively. The β-Sn grains are set as hexagonal shapes with a side length of 3 μm such that the β-Sn grain boundaries (GB) meeting at a triple junction are oriented at 120° with respect to each other.

### B. Modeling Technique for Microstructural Evolution

The four phases in the system are represented by a set of nonconserved order parameters  $\eta_{\rho i}$ , whose values range

from 0 to 1. The first subscript,  $\rho$ , refers to the phase, and the second,  $i$ , refers to the crystallographic orientation. Using  $\eta_{\rho i}$ , the phase fraction  $\phi_\rho$  at any location can be calculated according to the following relationship [29]:

$$\phi_\rho = \frac{\sum_{i=1}^{n_\rho} \eta_{\rho i}^2}{\sum_{\alpha=1}^4 \sum_{i=1}^{n_\alpha} \eta_{\alpha i}^2}, \quad (1)$$

where  $n_\rho$  is the number of orientations set for phase  $\rho$  and  $\phi_\rho(X)=1$  indicates that location  $X$  is fully occupied by phase  $\rho$ . In addition to  $\eta_{\rho i}$ , another set of variables is required to account for the interdiffusion process: the local mole fraction of Sn, denoted as  $c$ , and the mole fraction of Sn in different phases, denoted as  $c_\rho$ . The mole fractions and the phase fractions are inter-related [29]:

$$c = \sum_{\rho=1}^4 \phi_\rho c_\rho. \quad (2)$$

The temporal evolution of the two sets of variables is driven by minimizing the free-energy functional of the system as follows [30]:

$$F = \int_V f_{int} + f_{chem} + f_{mech} + f_{elec} + \mu(c - \sum_{\rho=1}^4 \phi_\rho c_\rho) dV, \quad (3)$$

where  $f_{int}$ ,  $f_{chem}$ ,  $f_{mech}$ , and  $f_{elec}$  are the interfacial, chemical, mechanical, and electrical free-energy densities, respectively; the last term in the integral is used to impose the constraint (2), and  $\mu$  is a Lagrange multiplier, which is also the interdiffusion potential [30]. The values of  $f_{int}$ ,  $f_{chem}$ ,  $f_{mech}$  and  $f_{elec}$  are calculated as follows [23], [26], [29]:

$$f_{int} = m \left[ \sum_{\rho=1}^4 \sum_{i=1}^{n_\rho} \left( \frac{\eta_{\rho i}^4}{4} - \frac{\eta_{\rho i}^2}{2} + \sum_{\alpha=1}^4 \sum_{j=1, \alpha j \neq \rho}^{n_\alpha} \gamma_{\rho i, \alpha j} \eta_{\rho i}^2 \eta_{\alpha j}^2 \right) + \frac{1}{4} \right] + \frac{\kappa}{2} \sum_{\rho=1}^4 \sum_{i=1}^{n_\rho} (\nabla \eta_{\rho i})^2, \quad (4)$$

$$f_{chem} = \sum_{\rho} \phi_\rho f_\rho, \quad (5)$$

$$f_{mech} = \frac{1}{2} (\epsilon_{kl} - \epsilon_{kl}^*) \left( \sum_{\rho=1}^4 \sum_{i=1}^{n_\rho} \eta_{\rho i} C_{\rho i, k l r s} \left/ \sum_{\rho=1}^4 \sum_{i=1}^{n_\rho} \eta_{\rho i} \right. \right) (\epsilon_{rs} - \epsilon_{rs}^*), \quad (6)$$

$$f_{elec} = \sum_{\rho=1}^4 \phi_\rho \rho_\rho^e \psi^e = -\frac{F^e \psi^e}{V_m} \sum_{\rho=1}^4 \phi_\rho [c_\rho Z_\rho^{Sn} + (1-c_\rho) Z_\rho^{Cu}], \quad (7)$$

where  $m$ ,  $\gamma_{\rho i, \alpha j}$ , and  $\kappa$  are constants related to the energy and thickness of the grain boundaries or the interfaces between different phases;  $f_\rho$  is the chemical free-energy density of phase  $\rho$  retrieved from a thermodynamic database developed by NIST [31];  $\rho_\rho^e$  is the electrical charge density of phase  $\rho$ ;  $\psi^e$  is the electric potential;  $Z_\rho^{Sn}$  and  $Z_\rho^{Cu}$  are the effective charge numbers of Sn and Cu in phase  $\rho$ , respectively;  $F^e$  is Faraday's constant;  $V_m=6.71 \times 10^{-5} \text{ m}^3/\text{mol}$  is the average molar volume of the system;  $\epsilon_{kl}$  is the total strain tensor;

$C_{\rho i,klrs}$  is the stiffness tensor of phase  $\rho$  with orientation  $i$ ; and  $\epsilon_{kl}^*$  is the eigenstrain tensor arising from the Cu dilatation effect, i.e., the volume expansion caused by the supersaturation of Cu atoms in the phases. The formula used by Chen [23] to calculate the eigenstrain of a two-phase system is extended to a multiphase system as follows:

$$\epsilon_{kl}^* = \left( c - \sum_{\rho=1}^4 \phi_{\rho} c_{\rho}^{eq} \right) \epsilon^c I, \quad (8)$$

where  $\epsilon^c = -0.01$ ;  $c_{\rho}^{eq}$  is the value of  $c_{\rho}$  when phase  $\rho$  is in thermodynamic equilibrium; and  $I = \begin{pmatrix} 1 & 0 \\ 0 & 1 \end{pmatrix}$ , indicating that the eigenstrain  $\epsilon_{kl}^*$  is assumed to be an isotropic volume strain. The Lagrange multiplier  $\mu$  can be obtained by solving  $\delta F/\delta c_{\rho}=0$  for  $\rho=1, 2, 3, 4$  together with (2) and (8), which results in the following equation:

$$\mu = \frac{\partial f'_1}{\partial c_1} - \epsilon^c \sigma_H = \frac{\partial f'_2}{\partial c_2} - \epsilon^c \sigma_H = \frac{\partial f'_3}{\partial c_3} - \epsilon^c \sigma_H = \frac{\partial f'_4}{\partial c_4} - \epsilon^c \sigma_H, \quad (9)$$

where  $f'_{\rho} = f_{\rho} + \rho_{\rho}^e \psi^e$  and  $\sigma_H$  is the hydrostatic stress. Equation (9) indicates that a local mechano-electro-chemical equilibrium is assumed, where  $\mu$  is the interdiffusion potential. It can be noted that  $\mu$  is irrelevant to the deviatoric stress, because  $I$  in (8) is assumed to be a unit matrix. If the off-diagonal components of  $I$  are not equal to zero, the contribution of the stress to  $\mu$ , i.e.,  $\epsilon^c \sigma_H$ , should be replaced by  $\epsilon^c I_{kl} \sigma_{kl}$ , where  $\sigma_{kl} = \sum_{\rho=1}^4 \sum_{i=1}^{n_{\rho}} \eta_{\rho i} C_{\rho i,klrs} / \sum_{\rho=1}^4 \sum_{i=1}^{n_{\rho}} \eta_{\rho i} (\epsilon_{rs} - \epsilon_{rs}^*)$  is the stress tensor. Based on (1)-(9), the governing equations for the microstructural evolution can be written as follows [29]:

$$\begin{aligned} \frac{\partial \eta_{\rho i}}{\partial t} &= -L \frac{\delta F}{\delta \eta_{\rho i}} \\ &= -L \left\{ m \left( \eta_{\rho i}^3 - \eta_{\rho i} + 2\eta_{\rho i} \sum_{\alpha=1}^4 \sum_{j=1, \alpha j \neq \rho i}^{n_{\alpha}} \gamma_{\rho i, \alpha j} \eta_{\alpha j}^2 \right) \right. \\ &\quad - \kappa \nabla^2 \eta_{\rho i} + \frac{2\eta_{\rho i}}{\sum_{\alpha=1}^4 \sum_{j=1}^{n_{\alpha}} \eta_{\alpha j}^2} \left[ (1 - \phi_{\rho}) (f'_{\rho} - \mu c_{\rho}) \right. \\ &\quad \left. \left. - \sum_{\alpha \neq \rho} \phi_{\alpha} (f'_{\alpha} - \mu c_{\alpha}) + (f_{\rho i,mech} - f_{mech}) \right] \right\}, \quad (10) \end{aligned}$$

$$\frac{\partial c}{\partial t} = \nabla \cdot \left( M \nabla \frac{\delta F}{\delta c} \right) = \nabla \cdot (M \nabla \mu), \quad (11)$$

where  $L=1.60 \times 10^{-9}$  m·s/kg is a constant related to the GB mobility;  $M$  is the interdiffusion mobility, which is proportional to the interdiffusion coefficients of Sn, i.e.,  $M=D/(\partial^2 f_{chem}/\partial c^2|_{c_{\rho}^{eq}})$ , and  $f_{\rho i,mech}=(\epsilon_{kl}-\epsilon_{kl}^*)C_{\rho i,klrs}(\epsilon_{rs}-\epsilon_{rs}^*)/2$  is the strain energy of phase  $\rho$  with orientation  $i$  under the total elastic strain. The interdiffusion coefficient  $D$  at the grain boundaries or the interfaces between different phases is set to 100 times the interdiffusion coefficient in the interior of the grains. Finally, the stress and electric potential are calculated by solving the equation for the stress equilibrium and the continuity equation of a steady-state current at every time step of the

TABLE I  
THE BOUNDARY CONDITIONS FOR THE GOVERNING EQUATIONS OF THE MODEL

Equation	Boundary	Boundary Condition
Phase field, (10) and (11)	all	no flux
	left and right	free deformable
Stress equilibrium, (12)	top	a stress along the $X$ -axis or $Y$ -axis
	bottom	fixed
Continuity equation of a steady-state current, (13)	left and right	electrically insulated
	top	an inflowing current along the $Y$ -axis
	bottom	grounded

simulation [23], [26]:

$$\frac{\partial \sigma_{ij}}{\partial x_i} = 0, \quad (12)$$

$$\nabla \cdot \left( \frac{\nabla \psi^e}{\sum_{\rho=1}^4 \phi_{\rho} \rho_{\rho}^r} \right) = 0, \quad (13)$$

where  $\sigma_{ij}=C_{ijkl}\epsilon_{kl}$  is the stress tensor and  $\rho_{\rho}^r$  is the electrical resistivity of phase  $\rho$ .

The boundary conditions for the governing equations, i.e., (10)-(13), are listed in Table I. Three boundary conditions for the external stress, i.e., tensile, compressive, and shear stresses, are considered in this study. These conditions can occur due to thermal expansion mismatch between chips and interconnects, warpage of the chips, or misalignment of the microbumps [32]–[34]. The magnitude of the stress applied to the top boundary of the Cu/Sn-microbump/Cu structure ranges from 300 MPa to 2 GPa. This high stress, which may not occur in real microbumps, is used in this study to highlight the effects of stress on microstructure.

### C. Material Parameters

The material parameters of the model are set in reference to the published experimental data [28], [35]–[41] and are listed in Table II. An isotropic interdiffusion coefficient for Sn,  $D$ , is used in studies of the interaction between external stresses and microstructural evolution. The interdiffusion coefficient is calculated using the intrinsic diffusion coefficients of Sn and Cu reported by Chao *et al.* [36] and the formula for calculating interdiffusion coefficients derived by Darken [42]. For the multiple grains of all phases considered in this model, various crystallographic orientations are established. The orientations of the  $\beta$ -Sn grains are represented by a set of Eulerian angles  $(\theta, \phi, \psi)$ , as schematically plotted in Fig. 2, where the two-dimensional domain of the Cu/Sn-microbump/Cu structure is located in the  $XOY$  plane. The orientation-dependent physical properties of the phases in the  $XOY$  plane, e.g., the stiffness tensor and the interdiffusion coefficient matrix, are obtained by rotating the tensors of the physical properties in 3D space according to the Eulerian angle  $(\theta, \phi, \psi)$  and then calculating the  $X$  and  $Y$  components of the rotated tensors.

TABLE II  
MATERIAL PARAMETERS USED IN THE MODEL\*

Phase	D (m <sup>2</sup> /s)	C <sub>11</sub> (GPa)	C <sub>22</sub> (GPa)	C <sub>33</sub> (GPa)	C <sub>44</sub> (GPa)	C <sub>55</sub> (GPa)	C <sub>66</sub> (GPa)	C <sub>12</sub> (GPa)	C <sub>13</sub> (GPa)
$\beta$ -Sn	$2.00 \times 10^{-15}$	75.29	75.29	95.52	21.93	21.93	23.36	61.56	44.99
Cu <sub>6</sub> Sn <sub>5</sub>	$1.61 \times 10^{-16}$	168.57	165.39	86.08	45.95	54.7	45.98	69.11	67.15
Cu <sub>3</sub> Sn	$2.87 \times 10^{-17}$	204.84	164.50	218.98	60.73	64.01	39.25	94.18	106.43
$\alpha$ -Cu	$8.00 \times 10^{-19}$	169.00	169.00	169.00	75.30	75.30	75.30	122.00	122.00
		C <sub>23</sub> (GPa)	C <sub>15</sub> (GPa)	C <sub>25</sub> (GPa)	C <sub>35</sub> (GPa)	C <sub>46</sub> (GPa)	$\rho_{\rho}^r$ ( $\times 10^{-8}$ Ω· m)	Z <sub>Sn</sub>	Z <sub>Cu</sub>
$\beta$ -Sn	44.00	0	0	0	0	13.3(a-axis), 20.3(c-axis)	18	3.25	
Cu <sub>6</sub> Sn <sub>5</sub>	67.59	17.02	34.45	28.05	-2.92	17.5	36	26	
Cu <sub>3</sub> Sn	106.40	0	0	0	0	8.9	23.6	26.5	
$\alpha$ -Cu	122.00	0	0	0	0	1.7	18	7	

\* D is the interdiffusion coefficient [36],  $C_{ij}$  is the stiffness tensor in Voigt notation [35], [40], [41],  $\rho_{\rho}^r$  is the electrical resistivity [37]–[39],  $Z_{Sn}$  and  $Z_{Cu}$  are the effective charge numbers of Sn and Cu, respectively [36].

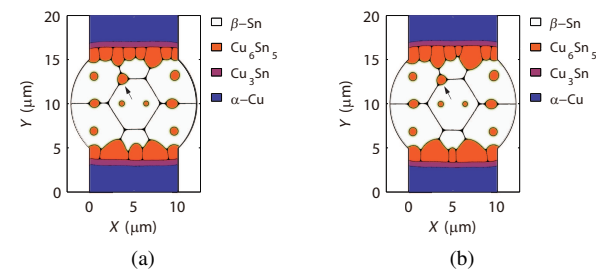
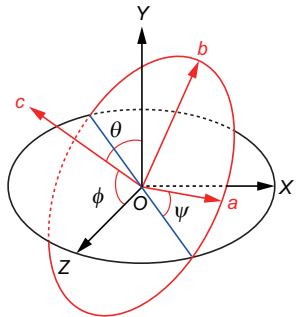


Fig. 2. A schematic plot of the Eulerian angles ( $\theta$ ,  $\phi$ ,  $\psi$ ) used to represent the orientation of the  $\beta$ -Sn grains. The Cu/Sn-microbump/Cu structure is located in the  $XOY$  plane.

### III. RESULTS AND DISCUSSION

#### A. Effects of Stress on the Morphology and Growth Rate of Interfacial IMCs

The microstructure in a Cu/Sn-microbump/Cu structure free of stress after isothermal aging at 150°C for 6000 s is shown in Fig. 3(a). This microstructure will be used as a benchmark for comparisons with the microstructure in the microbumps formed under stress to clearly reveal the effects of stress on microstructural evolution. An external tensile stress in the positive  $Y$  direction with a magnitude of  $\sigma_Y=2$  GPa and a compressive stress in the negative  $Y$  direction with a magnitude of  $\sigma_Y=-1$  GPa are applied to the top boundary of the structure, resulting in the microstructures observed in Figs. 3(b) and (c).

A root mean square (RMS) roughness parameter, defined as follows, is used to represent the morphology of the interfacial Cu<sub>6</sub>Sn<sub>5</sub> grains [43]:

$$R_{rms} = \sqrt{\sum_{i=1}^N (Y_i - \bar{Y})^2 / N}, \quad (14)$$

where  $N$  is the number of sampling points on the interface between the interfacial Cu<sub>6</sub>Sn<sub>5</sub> grains and the  $\beta$ -Sn grains;  $Y_i$  is the  $Y$  coordinate of the  $i$ th sampling point; and  $\bar{Y}$  is the average value of  $Y_i$ . It has been observed that the roughness of the interfacial Cu<sub>6</sub>Sn<sub>5</sub> grains under tensile stress, i.e., 0.37  $\mu\text{m}$ , is similar to their roughness in the stress-free case, i.e.,

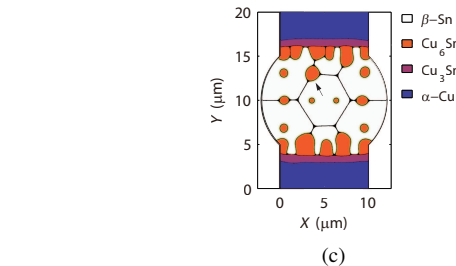


Fig. 3. The microstructure of the Cu/Sn-microbump/Cu structure under (a) a stress-free condition, (b) a tensile stress of  $\sigma_Y=2$  GPa, and (c) a compressive stress of  $\sigma_Y=-1$  GPa at  $T=150^\circ\text{C}$  and  $t=6000$  s.

0.30  $\mu\text{m}$ . In contrast, when compressive stress is applied, the interfacial Cu<sub>6</sub>Sn<sub>5</sub> grains are transformed from a continuous layer into many separated Cu<sub>6</sub>Sn<sub>5</sub> grains, as illustrated in Fig. 3(c), whose roughness is 0.62  $\mu\text{m}$ . The tensile stress also results in a slightly smaller bulk Cu<sub>6</sub>Sn<sub>5</sub> particle sitting at the triple junction of the  $\beta$ -Sn GBs, indicated by the arrow in Fig. 3(b), whereas the bulk Cu<sub>6</sub>Sn<sub>5</sub> particle marked by the arrow in Fig. 3(c) is larger under compressive stress.

In addition to morphology, stress also affects the growth rates of the interfacial Cu<sub>6</sub>Sn<sub>5</sub> and Cu<sub>3</sub>Sn grains. Fig. 4 plots thickness as a function of time for the interfacial Cu<sub>6</sub>Sn<sub>5</sub> grains, Cu<sub>3</sub>Sn grains, and Cu UBMs in the microbumps, as illustrated in Fig. 3. The thickness of each phase is calculated by averaging the thicknesses of the phase at the top and bottom of the microbump. As shown in Fig. 4(a), the growth of the interfacial Cu<sub>6</sub>Sn<sub>5</sub> grains is accelerated under tensile stress, but impeded under compressive stress. In contrast, Fig. 4(b) demonstrates that the interfacial Cu<sub>3</sub>Sn grains are thicker

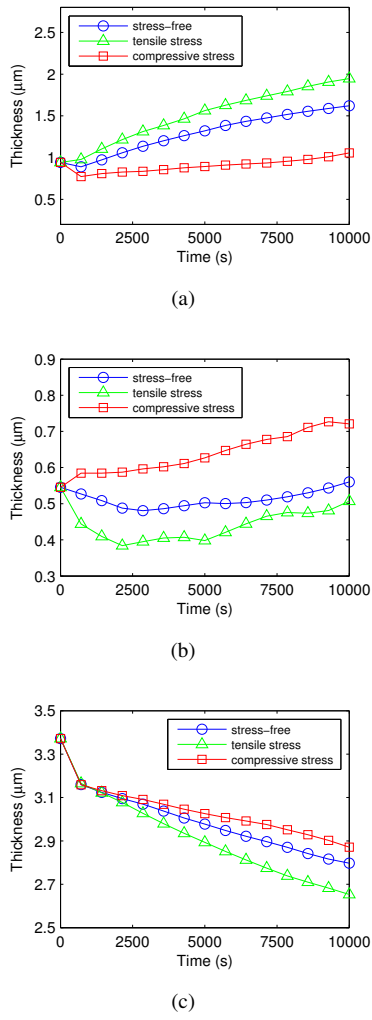


Fig. 4. The thicknesses of the interfacial (a) Cu<sub>6</sub>Sn<sub>5</sub> grains, (b) Cu<sub>3</sub>Sn grains, and (c) Cu UBMs as a function of time during the microstructural evolution of the Cu/Sn-microbump/Cu structure in Fig. 3.

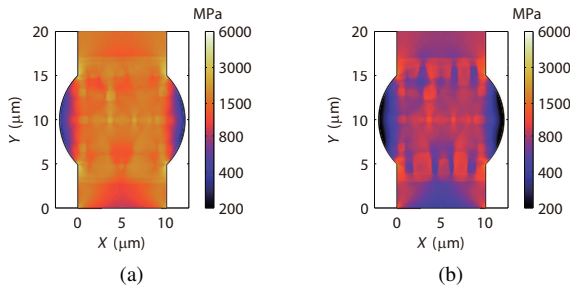


Fig. 5. The distribution of the von Mises stress in the Cu/Sn-microbump/Cu structure. The microstructures corresponding to (a) and (b) are shown in Figs. 3(b) and (c), respectively.

under compressive stress but thinner under tensile stress. The change in thickness of the interfacial Cu<sub>6</sub>Sn<sub>5</sub> grains is greater than the change in thickness of the interfacial Cu<sub>3</sub>Sn grains; therefore, the entire IMC layer consisting of both Cu<sub>6</sub>Sn<sub>5</sub> and Cu<sub>3</sub>Sn is thicker under tensile stress, resulting in faster consumption of the Cu UBMs, as illustrated in Fig. 4(c).

Two factors incorporated in our model may affect the

microstructural evolution. One is the difference in the strain energy caused by the difference in the Young's moduli of the phases, hereinafter called the "strain energy factor". Under external stress, higher von Mises stresses tend to concentrate in phases with larger Young's moduli, i.e., the Cu<sub>6</sub>Sn<sub>5</sub> and Cu<sub>3</sub>Sn phases in Figs. 5(a) and (b). Such a stress concentration results in a higher strain energy in the Cu<sub>6</sub>Sn<sub>5</sub> and Cu<sub>3</sub>Sn phases than in the β-Sn and α-Cu phases. When a phase with a smaller Young's modulus, e.g., β-Sn, is transformed into a phase with a larger Young's modulus, e.g., Cu<sub>6</sub>Sn<sub>5</sub>, the change in the strain energy will be  $f_{Cu_6Sn_5,mech} - f_{\beta-Sn,mech} > 0$ . In this case, the kinetics  $\partial \eta_{Cu_6Sn_5} / \partial t$  will slow down according to (10), i.e., the growth of the Cu<sub>6</sub>Sn<sub>5</sub> phase will be slower than that in the stress-free condition. Therefore, the difference in the strain energy of the phases cannot explain the enhanced growth of the interfacial Cu<sub>6</sub>Sn<sub>5</sub> phase under tensile stress as illustrated in Fig. 3(b). The different morphologies of the Cu<sub>6</sub>Sn<sub>5</sub> and Cu<sub>3</sub>Sn phases in Figs. 3(b) and (c) should be attributed to another factor, i.e., the interdiffusion of Sn and Cu driven by the gradient of the hydrostatic stress. This factor is hereinafter called the "stress gradient factor". According to (9) and (11), the interdiffusion flux is written as follows:

$$j = -M [\nabla(\partial f'_1 / \partial c_1) - \epsilon^c \nabla \sigma_H]. \quad (15)$$

The mole fraction of Sn is distributed homogeneously inside the grains of each phase and varies only at the interfaces between different phases before a stress is applied. Therefore,  $\nabla(\partial f'_1 / \partial c_1)$  vanishes inside the grains, and thus, the gradient of the hydrostatic stress  $\sigma_H$  will promote interdiffusion after a stress is applied according to (15). More specifically, the interdiffusion flux tends to flow toward locations with a lower tensile stress, i.e., a smaller value of  $|\sigma_H|$  when  $\sigma_H > 0$ , or a higher compressive stress, i.e., a larger value of  $|\sigma_H|$  when  $\sigma_H < 0$ , because  $\epsilon^c < 0$  is assumed in the model. The redistribution of Sn due to the interdiffusion driven by the stress gradient in turn changes the strain energy and chemical energy and thus affects the evolution of the order parameters  $\eta_{\rho_i}$  according to (5), (8), (9), and (10).

To more clearly demonstrate the interdiffusion driven by the stress gradient, a simpler system with only two Cu<sub>6</sub>Sn<sub>5</sub> grains between a β-Sn and a Cu<sub>3</sub>Sn grain in a rectangular domain is studied. The initial setting and boundary conditions of the model are shown in Fig. 6(a). The top boundary of the system is stretched or compressed along the Y direction by a stress of 1 GPa. Figs. 6(b) and (c) show the microstructures formed under tensile and compressive stresses, respectively, at  $t=1000$  s. The distributions of the hydrostatic stress in the systems in Figs. 6(b) and (c) are presented in Figs. 6(f) and (g), respectively, where the streamlines represent the interdiffusion flux. The stress distributions in the system are not homogeneous when external stresses are applied due to the difference in the Young's moduli of the phases. In Fig. 6(f), the hydrostatic stress over the entire domain is observed to be tensile, i.e.,  $\sigma_H > 0$ , with the minimum tensile stress located in the region that separates the two Cu<sub>6</sub>Sn<sub>5</sub> grains. The interdiffusion flux tends to flow away from the top boundary and into the region between the two Cu<sub>6</sub>Sn<sub>5</sub> grains, which is driven by the gradient of  $\sigma_H$  according to (15). Consequently,

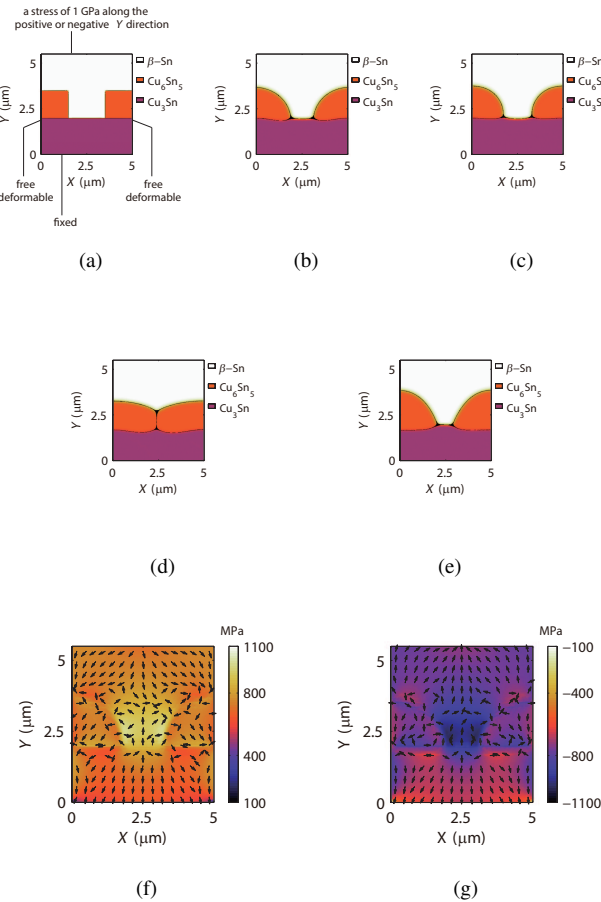


Fig. 6. The effect of stress on the morphological evolution of two Cu<sub>6</sub>Sn<sub>5</sub> grains between a  $\beta$ -Sn and a Cu<sub>3</sub>Sn grain at  $T=150^\circ\text{C}$ . (a) The initial microstructure and the boundary conditions. (b) and (d) The microstructure formed under a tensile stress of  $\sigma_Y=1$  GPa at  $t=1000$  s and 10000 s, respectively. (c) and (e) The microstructure formed under a compressive stress of  $\sigma_Y=-1$  GPa at  $t=1000$  s and 10000 s, respectively. (f) and (g) The distributions of the hydrostatic stress in (b) and (c), respectively, with the streamlines indicating the interdiffusion flux.

more Sn atoms are available at the interface between the  $\beta$ -Sn and Cu<sub>3</sub>Sn grains to react and form a new Cu<sub>6</sub>Sn<sub>5</sub> phase. Therefore, the two Cu<sub>6</sub>Sn<sub>5</sub> grains grow toward each other and become a continuous layer, as illustrated in Fig. 6(d). In contrast, the maximum compressive stress is observed in the region between the two Cu<sub>6</sub>Sn<sub>5</sub> grains as depicted in Fig. 6(g) when the compressive stress is applied. In this case, the interdiffusion flux is driven away from the region that separates the two Cu<sub>6</sub>Sn<sub>5</sub> grains by the stress gradient. Therefore, the growth of the two Cu<sub>6</sub>Sn<sub>5</sub> grains near the region is impeded, and thus, the grains remain separated by the  $\beta$ -Sn grain up to  $t=10000$  s, as shown in Fig. 6(e).

### B. Effects of Stress on the Orientation Evolution of the $\beta$ -Sn Grains

An external compressive stress in the negative  $Y$  direction with a magnitude of  $\sigma_Y=-300$  MPa and an external shear stress in the positive  $X$  direction with a magnitude of  $\sigma_X=300$  MPa are applied to the top boundary of the Cu/Sn-microbump/Cu structure without bulk Cu<sub>6</sub>Sn<sub>5</sub> particles.

The effect of stress on the preferential orientation of the  $\beta$ -Sn grains is illustrated in Fig. 7. Fig. 7(a) shows the initial microstructure, and Fig. 7(b) plots the orientations of the  $\beta$ -Sn grains in Fig. 7(a), which are represented by the angle between the  $Y$  direction and the  $c$ -axis, i.e., the angle  $\theta$ . Three different orientations represented by the Eulerian angles of (90°, 0°, 0°), (60°, 90°, 90°), and (30°, 90°, 90°) are set for the  $\beta$ -Sn grains, denoted as the G1, G2, and G3 grains in Fig. 7(b). That is, the  $\theta$  angles of the G1, G2, and G3 grains are 90°, 60°, and 30°, respectively. Figs. 7(c) and (d) show the microstructure and the corresponding  $\beta$ -Sn grain orientations in a microbump free of stress at  $t=10000$  s, where the morphology of the  $\beta$ -Sn grains is nearly symmetric about the line  $Y=10$  μm. In contrast, the preferential orientation of the G1 grains is observed when an external stress is applied. Figs. 7(e) and (g) show the microstructure within the microbumps under a compressive stress of  $\sigma_Y=-300$  MPa and a shear stress of  $\sigma_X=300$  MPa, respectively, with the corresponding orientations of the  $\beta$ -Sn grains shown in Figs. 7(f) and (h). Both Figs. 7(f) and (h) suggest that the G1 grains grow faster with the consumption of the G2 and G3 grains. In particular, the G1 grains completely consume the G2 and G3 grains and merge into one grain in the microbump under the shear stress, as illustrated in Fig. 7(h). This result is comparable to experimental observations, such that the  $c$ -axis of the  $\beta$ -Sn grains is rotated in the direction parallel to the solder-UBM interface in response to the shear stress generated during thermal cycling [13].

The evolution of the order parameter of the  $\beta$ -Sn grains with the  $i$ th orientation, i.e.,  $\partial\eta_{\beta-Sni}/\partial t$ , is determined by the interfacial energy and strain energy according to (10) because  $\phi_{\beta-Sn}$  equals 1 and  $\phi_\alpha$  equals 0 within the  $\beta$ -Sn grains and at the  $\beta$ -Sn GBs. Due to its body-centered tetragonal crystal structure,  $\beta$ -Sn has stronger anisotropy than the other phases. The anisotropic stiffness tensor of  $\beta$ -Sn causes a relatively lower von Mises stress in the two G1 grains in the top half of the microbumps than in the G2 grains in the tensile or compressive stress scenarios, as shown in Figs. 8(a) and (b). Therefore, the two G1 grains have lower strain energy than the G2 grains, which promotes the growth of the former, as illustrated in Figs. 7(f) and (h).

The effect of compressive stress on the morphology of the interfacial Cu<sub>6</sub>Sn<sub>5</sub> grains is consistent with the result discussed in Section III-A. That is, the compressive stress increases the roughness of the interface between the interfacial Cu<sub>6</sub>Sn<sub>5</sub> grains and the  $\beta$ -Sn grains, as can be observed by comparing Figs. 7(c) and (e). In contrast, the morphology of the Cu<sub>6</sub>Sn<sub>5</sub> grains at the top interface of the microbump is not clearly altered when shear stress is applied. However, the Cu<sub>6</sub>Sn<sub>5</sub> grains adjacent to the left and right boundaries at the bottom interface of the microbump are consumed by the  $\beta$ -Sn phase because higher stress concentrates at the two locations marked by the arrows in Fig. 8(b), which increases the strain energy of the Cu<sub>6</sub>Sn<sub>5</sub> grains at these locations.

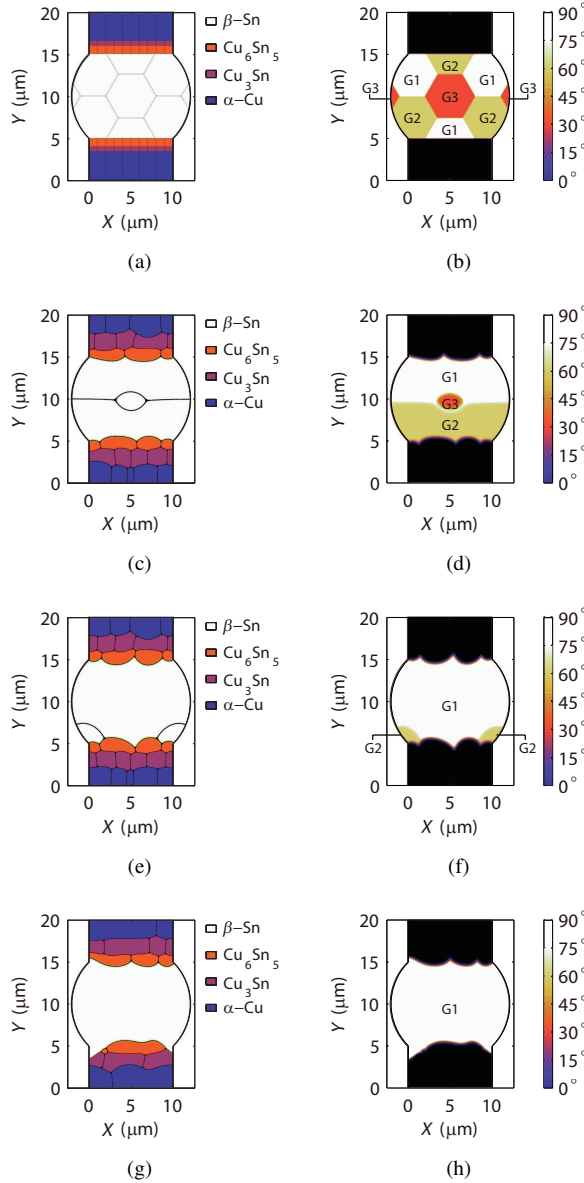


Fig. 7. The effect of stress on the preferential orientation of the  $\beta$ -Sn grains. (a) The initial microstructure. The microstructure formed under (c) a stress-free condition, (e) a compressive stress of  $\sigma_Y = -300$  MPa, and (g) a shear stress of  $\sigma_X = 300$  MPa at  $T = 150^\circ\text{C}$  and  $t = 10000$  s. (b), (d), (f), and (h) The angle between the  $Y$  direction and the  $c$ -axis of the  $\beta$ -Sn grains in (a), (c), (e), and (g), respectively.

### C. Effects of Electromigration on Orientation Evolution of $\beta$ -Sn Grains

In addition to the external stresses, EM is also a process that affects the microstructural evolution within microbumps. The combined effects of EM and the internal stress caused by EM on the microstructure of the Cu/Sn-microbump/Cu structure are discussed in this section. An electric current in the negative  $Y$  direction,  $j_Y = -1.27 \times 10^4$  A/cm $^2$ , is imposed at the top boundary of the microbumps. The initial microstructure and orientations of the  $\beta$ -Sn grains in the model are shown in Figs. 9(a) and (b), respectively. Three different orientations are set for the  $\beta$ -Sn grains, i.e., the G4, G5, and G6 grains with the Eulerian angles  $(0^\circ, 90^\circ, 0^\circ)$ ,  $(90^\circ, 90^\circ, 90^\circ)$ , and

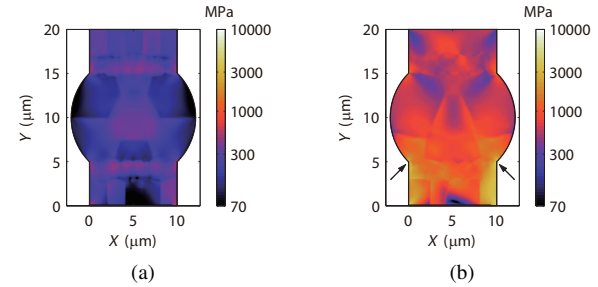


Fig. 8. The distribution of the von Mises stress in the Cu/Sn-microbump/Cu structure at  $t = 1000$  s under (a) a compressive stress of  $\sigma_Y = -300$  MPa and (b) a shear stress of  $\sigma_X = 300$  MPa.

$(60^\circ, 45^\circ, 90^\circ)$ , respectively, as shown in Fig. 9(b). Both the electrical resistivity  $\rho_p^r$  and the interdiffusion coefficient  $D$  of the  $\beta$ -Sn grains are dependent on the orientations. A special case considering the anisotropy of the interdiffusion coefficient  $D$ , i.e.,  $D_c = 500D_a$ , is studied, and the microstructures formed at  $t = 10000$  s are shown in Fig. 9(c). The roughness of the  $\beta$ -Sn- $\text{Cu}_6\text{Sn}_5$  interface adjacent to the G4 grain of the microbump is greater than the roughness adjacent to the G5 and G6 grains. This result is most likely due to the faster interdiffusion along the  $Y$  direction in the G4 grain, according to the study by Hong *et al.* on the morphology of interfacial  $\text{Cu}_6\text{Sn}_5$  grains under a stress-free condition [27]. The roughness of the interface at the anode of the microbump in Fig. 9(c) is  $0.67 \mu\text{m}$ , which is controlled by the interdiffusion flux driven by EM. The current density is higher in the G5 and G6 grains than in the G4 grain because the electrical resistivity along the  $c$ -axis of the  $\beta$ -Sn grain is greater than the electrical resistivity along the  $a$ -axis by approximately 53% according to Table II. The direction of the electric current is determined by the geometry of the microbump and is slightly affected by the anisotropy of the electrical resistivity. The interdiffusion flux caused by the EM process can be calculated as follows according to (7), (9), and (11):

$$j_{elec} = -MV\nabla \frac{\partial f_{elec}}{\partial c_1} = \frac{MF^e}{V_m} \phi_1 (Z_1^{Sn} - Z_1^{Cu}) \nabla \psi^e. \quad (16)$$

The effective charge densities of Sn and Cu in the  $\beta$ -Sn phase are  $Z_1^{Sn} = 18$  and  $Z_1^{Cu} = 3.25$ , respectively, as listed in Table II. Equation (16) indicates that the electric current flowing in the negative  $Y$  direction across the microbump drives the interdiffusion flux to flow in the same direction, i.e., toward the cathode. The interdiffusion driven by EM along the  $\text{Cu}_6\text{Sn}_5$  GBs is faster than the interdiffusion within the  $\text{Cu}_6\text{Sn}_5$  grains, resulting in fewer Sn atoms available for the growth of the  $\text{Cu}_6\text{Sn}_5$  grains near the  $\text{Cu}_6\text{Sn}_5$  GBs. Therefore, the roughness of the interface at the anode is increased as the roughness of the interface at the cathode is decreased.

Fig. 9(d) shows the orientations of the  $\beta$ -Sn grains in Figs. 9(c). It is evident that most of the  $\beta$ -Sn grains are occupied by G4 grains after EM for 10000 s. This result indicates that the  $\beta$ -Sn grains with their  $c$ -axis parallel to the direction of the electric current tend to grow preferentially when  $D_c = 500D_a$ . This difference in the interdiffusion coefficients of two neighboring  $\beta$ -Sn grains results in a variation in the interdiffusion

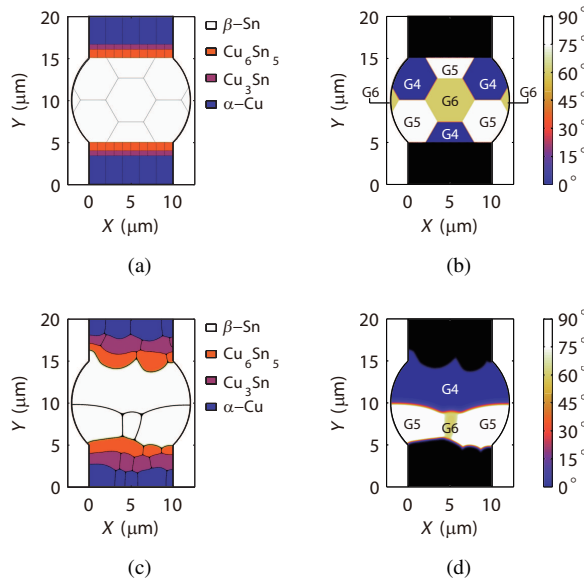


Fig. 9. The combined effect of EM and stress on the morphological evolution of the interfacial  $\text{Cu}_6\text{Sn}_5$  and  $\beta\text{-Sn}$  grains. (a) The initial microstructure. (c) The microstructure formed under an electric current of  $j_Y = -1.27 \times 10^4 \text{ A/cm}^2$  at  $t = 10000 \text{ s}$  and  $T = 150^\circ\text{C}$  for  $D_c = 500D_a$ . (b) and (d) The angle between the  $Y$  direction and the  $c$ -axis of the  $\beta\text{-Sn}$  grains in (a) and (c), respectively.

mobility  $M$  across the  $\beta\text{-Sn}$  GBs. Thus, the mole fraction of Sn at the GBs deviates from the mole fraction of Sn in the  $\beta\text{-Sn}$  grains according to the following equation derived from (11):

$$\frac{\partial c}{\partial t} = \nabla M \cdot \nabla \mu + M \nabla^2 \mu. \quad (17)$$

The deviation of the mole fraction of Sn causes strain at the  $\beta\text{-Sn}$  GBs according to (8). The strain favors the growth of the G4 grains because a replacement of the  $\beta\text{-Sn}$  GBs by the G4 grains can decrease the strain energy at the  $\beta\text{-Sn}$  GBs, which is calculated by the following expression:

$$(f_{G4,mech} - f_{mech})(\eta_{G4}\eta_{G5} + \eta_{G4}\eta_{G6}), \quad (18)$$

where  $f_{mech}$  is the strain energy density at any location in the microbump;  $f_{G4,mech}$  is the strain energy density when the grain or GB at the same location is completely transformed into a G4 grain; and  $(\eta_{G4}\eta_{G5} + \eta_{G4}\eta_{G6})$  is used to represent the GBs connected to the G4 grains, i.e.,  $(\eta_{G4}\eta_{G5} + \eta_{G4}\eta_{G6}) > 0$  at the GBs and  $(\eta_{G4}\eta_{G5} + \eta_{G4}\eta_{G6}) \rightarrow 0$  inside the  $\beta\text{-Sn}$  grains. The preferential orientation of  $\beta\text{-Sn}$  grains predicted in this section is different from the experimental result of Wu *et al.* [18], who observed the alignment of the  $c$ -axis perpendicular to the direction of the electric current. This difference most likely occurs because vacancy diffusion is not considered in this study. The distribution of the strain energy caused by vacancies is different from the distribution of the strain energy caused by the interdiffusion between Sn and Cu, because the interdiffusion between Sn and vacancies along the  $a$ -axis of the  $\beta\text{-Sn}$  grains is faster, i.e.,  $D_a > D_c$  [18]. In this case, the strain energy may be minimized by growing  $\beta\text{-Sn}$  grains with their  $c$ -axis perpendicular to the current direction.

#### D. Microstructure-dependent Shear Modulus of the Microbumps

The purpose of studying the microstructural evolution under stress is to directly predict the mechanical properties of the microbumps based on the simulated microstructure. In this section, a shear stress in the positive  $X$  direction, i.e.,  $\sigma_X = 10 \text{ MPa}$ , is applied to the top boundary of the microbumps with the simulated microstructure obtained in Sections III-A to III-C. Then, the shear modulus of the microbumps is calculated as follows:

$$G = (\sigma_X h) / d_X, \quad (19)$$

where  $\sigma_X$  is the shear stress imposed on the top boundary of the microbumps;  $d_X$  is the displacement of the top boundary along the  $X$  direction; and  $h$  is the standoff height. The shear modulus of the microbump is related to the orientation-dependent shear modulus of the four constituent phases, which is calculated as follows [44]:

$$G_{\rho i} = \frac{1}{4}(C_{11,\rho i} - C_{12,\rho i} + 2C_{44,\rho i}) \quad (20)$$

where  $C_{11,\rho i}$ ,  $C_{12,\rho i}$ , and  $C_{44,\rho i}$  are the components of the stiffness tensor of phase  $\rho$  with orientation  $i$  in Voigt notation. The stiffness tensor of each grain of phase  $\rho$  is obtained by rotating the stiffness tensor of phase  $\rho$  listed in Table II according to the Eulerian angles of the grain. The average shear modulus of a phase can be calculated as follows using (20):

$$\bar{G}_{\rho} = \sum_{i=1}^{n_{\rho}} G_{\rho i} / n_{\rho}, \quad (21)$$

where  $n_{\rho}$  is the number of crystallographic orientations set for phase  $\rho$ . Fig. 10 plots the shear modulus of the microbumps as a function of time during microstructural evolution from  $t = 0 \text{ s}$  to  $10000 \text{ s}$ . A slight increase in the shear modulus of the three microbumps is observed when bulk  $\text{Cu}_6\text{Sn}_5$  particles are considered. This increase is caused by the growth of the interfacial  $\text{Cu}_6\text{Sn}_5$  and  $\text{Cu}_3\text{Sn}$  grains. The average shear moduli of the  $\text{Cu}_6\text{Sn}_5$  and  $\text{Cu}_3\text{Sn}$  grains are calculated by (21) to be 50.6 GPa and 53.6 GPa, respectively, which are greater than the shear moduli of the  $\beta\text{-Sn}$  and  $\alpha\text{-Cu}$  grains, i.e., 19.6 GPa and 45.1 GPa, respectively. Therefore, it is more difficult to deform a microbump with thicker  $\text{Cu}_6\text{Sn}_5$  and  $\text{Cu}_3\text{Sn}$  grains by applying shear stress. However, the difference in the shear modulus of the three microbumps with bulk  $\text{Cu}_6\text{Sn}_5$  particles is negligible because the effect of stress on the thicknesses of the interfacial  $\text{Cu}_6\text{Sn}_5$  and  $\text{Cu}_3\text{Sn}$  grains is negligible, i.e., as small as  $<1 \mu\text{m}$ , as observed in Figs. 4(a) and (b). In contrast, when the bulk  $\text{Cu}_6\text{Sn}_5$  particles are not considered, the shear modulus of the microbump marked by the solid square symbols in Fig. 10 decreases by approximately 30% due to the faster growth of the G1 grains under the shear stress, as illustrated in Fig. 7(h). The shear moduli of the G1, G2, and G3 grains calculated by (20) are 14.4 GPa, 23.6 GPa, and 20.7 GPa, respectively. Therefore, the G1 grains deform more easily than the G2 and G3 grains under the same external shear stress. For the same reason, the preferential growth of the G1 grains under compressive stress, as shown in Fig. 7(f), also decreases the shear modulus of the microbump marked by

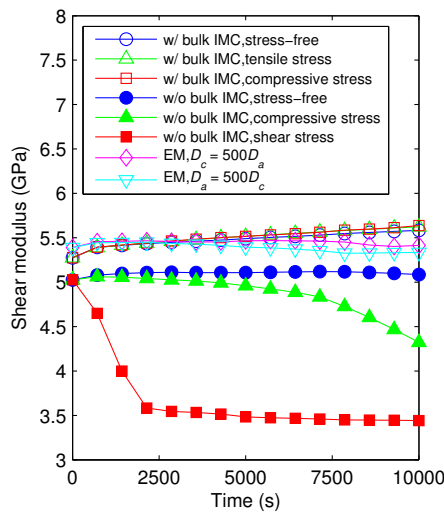


Fig. 10. The plots of the shear modulus of the Cu/Sn-microbump/Cu structure as a function of time during microstructural evolution under stress and EM.

the solid triangle symbols in Fig. 10. However, the decrease in the shear modulus of the microbump at  $t=10000$  s is smaller under compressive stress than under shear stress because the two G2 grains still exist in the microbump, as observed in Fig. 7(f). Finally, the shear modulus of the microbumps during EM also decreases due to the evolution of the morphology of the  $\beta$ -Sn grains; however, the decrease is only approximately 2% at  $t=10000$  s because the morphological evolution under EM is even slower than that under external stresses.

#### IV. CONCLUSION

The effects of external stress and EM on the microstructure of Cu/Sn-microbump/Cu structures at 150°C were studied using a phase-field model. The responses of the microstructures to stress and EM can be summarized as follows:

- 1) The morphology and thickness of interfacial  $\text{Cu}_6\text{Sn}_5$  grains are affected by the direction of the external stress applied: a compressive stress favors the separation of interfacial  $\text{Cu}_6\text{Sn}_5$  grains by  $\beta$ -Sn grains, whereas a tensile stress promotes the formation of a continuous layer of  $\text{Cu}_6\text{Sn}_5$  grains. The roughness of the  $\beta$ -Sn- $\text{Cu}_6\text{Sn}_5$  interface increases under compressive stress and decreases under tensile stress.
- 2)  $\beta$ -Sn grains with their  $c$ -axis perpendicular to the  $Y$  direction grow preferentially under an external shear or compressive stress.
- 3) The roughness of the interfacial  $\text{Cu}_6\text{Sn}_5$  grains at the cathode is increased by the interdiffusion flux driven by EM. In addition, the  $\beta$ -Sn grains with a larger interdiffusion coefficient along the direction in which the electric current flows grow faster under the EM-induced stress.
- 4) The decreases in the shear modulus of the microbumps under external stresses or EM are caused by the preferential growth of the  $\beta$ -Sn grains, which deform more easily under a shear load.

#### ACKNOWLEDGMENT

The authors wish to acknowledge the financial support received from the Pearl River Science and Technology Nova Program of Guangzhou under grant no. 2012J2200074 and the National Natural Science Foundation of China (NSFC) under grant no. 51004118.

#### REFERENCES

- [1] K.-B. Yeap, M. Roellig, R. Huebner, M. Gall, V. Sukharev, and E. Zschech, "A critical review on multiscale material database requirement for accurate three-dimensional IC simulation input," *IEEE Trans. Device Mater. Rel.*, vol. 12, no. 2, pp. 217–224, Jun. 2012.
- [2] T. Jiang, C. Wu, P. Su, X. Liu, P. Chia, L. Li, H.-Y. Son, J.-S. Oh, K.-Y. Byun, N.-S. Kim, J. Im, R. Huang, and P. Ho, "Characterization of plasticity and stresses in TSV structures in stacked dies using synchrotron X-ray microdiffraction," in *2013 IEEE 63rd Electron. Compon. Technol. Conf.*, pp. 641–647.
- [3] M. Nakamoto, R. Radojcic, Wei Zhao, V. Dasarapu, A. Karmarkar, and Xiaopeng Xu, "Simulation methodology and flow integration for 3D IC stress management," in *2010 IEEE Custom Integr. Circuits Conf.—CICC 2010*, p. 4 pp.
- [4] A. Kteyan, G. Gevorgyan, H. Hovsepyan, J.-H. Choy, and V. Sukharev, "Stress assessment for device performance in three-dimensional IC: linked package-scale/die-scale/feature-scale simulation flow," *J. Micro/Nanolith. MEMS MOEMS*, vol. 13, no. 1, p. 011203, Jan. 2014.
- [5] W. S. Yoo, J. H. Kim, and S. M. Han, "Multiwavelength raman characterization of silicon stress near through-silicon vias and its inline monitoring applications," *J. Micro/Nanolith. MEMS MOEMS*, vol. 13, no. 1, p. 011205, Feb. 2014.
- [6] A. Ivankovic, G. Van der Plas, V. Moroz, M. Choi, V. Cherman, A. Mercha, P. Marchal, M. Gonzalez, G. Eneman, W. Zhang, T. Buisson, M. Detalle, A. Manna, D. Verkest, G. Beyer, E. Beyne, B. Vandeveld, I. De Wolf, and D. Vandepitte, "Analysis of microbump induced stress effects in 3D stacked IC technologies," in *2011 IEEE International 3D Systems Integration Conference (3DIC)*, 2012 2012, p. 5 pp.
- [7] S.-K. Ryu, K.-H. Lu, T. Jiang, J.-H. Im, R. Huang, and P. S. Ho, "Effect of thermal stresses on carrier mobility and keep-out zone around through-silicon vias for 3-D integration," *IEEE Trans. Device Mater. Rel.*, vol. 12, no. 2, pp. 255–262, Jun. 2012.
- [8] M. Jung, D. Z. Pan, and S. K. Lim, "Chip/package mechanical stress impact on 3-D IC reliability and mobility variations," *IEEE Trans. Comput.-Aided Design Integr. Circuits Syst.*, vol. 32, no. 11, pp. 1694–1707, Nov. 2013.
- [9] V. Sukharev, "Beyond Black's equation: Full-chip EM/SM assessment in 3D IC stack," *Microelectron. Eng.*, vol. 120, pp. 99–105, May 2014.
- [10] V. Sukharev, A. Kteyan, J.-H. Choy, H. Hovsepyan, A. Markosian, E. Zschech, and R. Huebner, "Multi-scale simulation methodology for stress assessment in 3D IC: effect of die stacking on device performance," *J. Electron. Test.*, vol. 28, no. 1, pp. 63–72, Feb. 2012.
- [11] K. N. Tu and T. Tian, "Metallurgical challenges in microelectronic 3D IC packaging technology for future consumer electronic products," *Sci. China Technol. Sci.*, vol. 56, no. 7, pp. 1740–1748, Jul. 2013.
- [12] T.-K. Lee, B. Zhou, and T. R. Bieler, "Impact of isothermal aging and Sn grain orientation on the long-term reliability of wafer-level chip-scale package Sn-Ag-Cu solder interconnects," *IEEE Trans. Compon. Packag. Manuf. Technol.*, vol. 2, no. 3, pp. 496–501, Mar. 2012.
- [13] B. Zhou, G. Muralidharan, K. Kurumadalli, C. M. Parish, S. Leslie, and T. R. Bieler, "Microstructure and Sn crystal orientation evolution in Sn-3.5Ag lead-free solders in high-temperature packaging applications," *J. Electron. Mater.*, vol. 43, no. 1, pp. 57–68, Jan. 2014.
- [14] H. Chen, L. Wang, J. Han, M. Li, Q. Wu, and J. Kim, "Grain orientation evolution and deformation behaviors in Pb-free solder interconnects under mechanical stresses," *J. Electron. Mater.*, vol. 40, no. 12, pp. 2445–2457, Dec. 2011.
- [15] O. M. Abdelhadi and L. Ladani, "Effect of joint size on microstructure and growth kinetics of intermetallic compounds in solid-liquid interdiffusion Sn3.5Ag/Cu-substrate solder joints," *J. Electron. Packag.*, vol. 135, no. 2, p. 021004, Mar. 2013.
- [16] H.-M. Lin and J.-G. Duh, "Interfacial reaction between Sn-3.0Ag-0.5Cu liquid solder and Ni-xZn novel UBM layers," *Surf. Coat. Technol.*, vol. 206, no. 7, pp. 1941–1946, Dec. 2011.
- [17] J. Ke, H. Chuang, W. Shih, and C. Kao, "Mechanism for serrated cathode dissolution in Cu/Sn/Cu interconnect under electron current stressing," *Acta Mater.*, vol. 60, no. 5, pp. 2082–2090, Mar. 2012.

- [18] A. T. Wu, K. N. Tu, J. R. Lloyd, N. Tamura, B. C. Valek, and C. R. Kao, "Electromigration-induced microstructure evolution in tin studied by synchrotron X-ray microdiffraction," *Appl. Phys. Lett.*, vol. 85, no. 13, p. 2490, 2004.
- [19] M. Huang, F. Yang, N. Zhao, and X. Liu, "Solder volume effect on interfacial reaction between Sn-3.0Ag-0.5Cu solder balls and Cu substrates - experiment and simulation," *ECS Trans.*, vol. 52, no. 1, pp. 753–758, Mar. 2013.
- [20] V. Sukharev, A. Kleyan, and E. Zschech, "Physics-based models for EM and SM simulation in three-dimensional IC structures," *IEEE Trans. Device Mater. Rel.*, vol. 12, no. 2, pp. 272–284, Jun. 2012.
- [21] M. Erinc, P. Schreurs, and M. Geers, "Intergranular thermal fatigue damage evolution in SnAgCu lead-free solder," *Mech. Mater.*, vol. 40, no. 10, pp. 780–791, Oct. 2008.
- [22] Z. Wu, Z. Huang, Y. Ma, H. Xiong, and P. P. Conway, "Effects of the microstructure of copper through-silicon vias on their thermally induced linear elastic mechanical behavior," *Electron. Mater. Lett.*, vol. 10, no. 1, pp. 281–292, Jan. 2014.
- [23] L.-Q. Chen, "Phase-field models for microstructure evolution," *Annu. Rev. Mater. Res.*, vol. 32, no. 1, pp. 113–140, Aug. 2002.
- [24] I. Steinbach and M. Apel, "Multi phase field model for solid state transformation with elastic strain," *Phys. D*, vol. 217, no. 2, pp. 153–160, May 2006.
- [25] M. Gururajan and T. Abinandanan, "Phase field study of precipitate rafting under a uniaxial stress," *Acta Mater.*, vol. 55, no. 15, pp. 5015–5026, Sep. 2007.
- [26] J. Guyer, W. Boettinger, J. Warren, and G. McFadden, "Phase field modeling of electrochemistry. II. Kinetics," *Phys. Rev. E*, vol. 69, no. 2, p. 021604, Feb. 2004.
- [27] K. K. Hong and J. Y. Huh, "Phase field simulations of morphological evolution and growth kinetics of solder reaction products," *J. Electron. Mater.*, vol. 35, no. 1, pp. 56–64, Jan. 2006.
- [28] M. Park, M. Stephenson, C. Shannon, L. Cceres Daz, K. Hudspeth, S. Gibbons, J. Muoz-Saldaa, and R. Arryave, "Experimental and computational study of the morphological evolution of intermetallic compound ( $Cu_6Sn_5$ ) layers at the Cu/Sn interface under isothermal soldering conditions," *Acta Mater.*, vol. 60, no. 13–14, pp. 5125–5134, Aug. 2012.
- [29] N. Moelans, "A quantitative and thermodynamically consistent phase-field interpolation function for multi-phase systems," *Acta Mater.*, vol. 59, no. 3, pp. 1077–1086, Feb. 2011.
- [30] N. Moelans, "A phase-field model for multi-component and multi-phase systems," *Arch. Metall. Mater.*, vol. 53, no. 4, pp. 1149–1156, 2008.
- [31] U. Kattner and C. Handwerker, "Calculation of phase equilibria in candidate solder alloys," *Z. Metallkd.*, vol. 92, no. 7, pp. 740–746, Jul. 2001.
- [32] K. Tu, "Reliability challenges in 3D IC packaging technology," *Microelectron. Rel.*, vol. 51, no. 3, pp. 517–523, Mar. 2011.
- [33] M. Mariappan, Y. Imai, S. Kimura, T. Fukushima, J.-C. Bea, H. Kino, K.-W. Lee, T. Tanaka, and M. Koyanagi, "Deteriorated device characteristics in 3D-LSI caused by distorted silicon lattice," *IEEE Trans. Electron Devices*, vol. 61, no. 2, pp. 540–547, Feb. 2014.
- [34] Y.-L. Shen and R. Johnson, "Misalignment induced shear deformation in 3D chip stacking: A parametric numerical assessment," *Microelectron. Rel.*, vol. 53, no. 1, pp. 79–89, Jan. 2013.
- [35] Seung-Hyun Chae, B. Chao, Xuefeng Zhang, J. Im, and P. Ho, "Investigation of intermetallic compound growth enhanced by electromigration in Pb-free solder joints," in *2007 Electron. Compon. Technol. Conf.*, pp. 1442–1449.
- [36] B. Chao, S.-H. Chae, X. Zhang, K.-H. Lu, J. Im, and P. Ho, "Investigation of diffusion and electromigration parameters for Cu-Sn intermetallic compounds in Pb-free solders using simulated annealing," *Acta Mater.*, vol. 55, no. 8, pp. 2805–2814, May 2007.
- [37] J. Peng, F. Wu, H. Liu, L. Zhou, and Q. Pan, "Effects of thermal aging on the electrical resistance of Sn-3.5Ag micro SOH solder joints," in *2009 Int. Conf. Electron. Packag. Technol. & High Density Packag. (ICEPT-HDP 2009)*, pp. 1023–1026.
- [38] R. A. Matula, "Electrical resistivity of copper, gold, palladium, and silver," *J. Phys. Chem. Ref. Data*, vol. 8, no. 4, pp. 1147–1298, 1979.
- [39] A. T. Wu, A. M. Gusak, K. N. Tu, and C. R. Kao, "Electromigration-induced grain rotation in anisotropic conducting beta tin," *Appl. Phys. Lett.*, vol. 86, no. 24, p. 241902, 2005.
- [40] J. Chen, Y.-S. Lai, P.-F. Yang, C.-Y. Ren, and D.-J. Huang, "Structural and elastic properties of  $Cu_6Sn_5$  and  $Cu_3Sn$  from first-principles calculations," *J. Mater. Res.*, vol. 24, no. 07, pp. 2361–2372, Jul. 2009.
- [41] W. Dreyer and W. Müller, "Modeling diffusional coarsening in eutectic tin/lead solders: a quantitative approach," *Int. J. Solids Struct.*, vol. 38, no. 8, pp. 1433–1458, Feb. 2001.
- [42] L. S. Darken, "Diffusion, mobility and their interrelation through free energy in binary metallic systems," *Trans. AIME*, vol. 175, pp. 184–201, 1948.
- [43] D. Yu and L. Wang, "The growth and roughness evolution of intermetallic compounds of Sn-Ag-Cu/Cu interface during soldering reaction," *J. Alloy. Compd.*, vol. 458, no. 1–2, pp. 542–547, Jun. 2008.
- [44] I. Schmidt and D. Gross, "Directional coarsening in ni-base superalloys: analytical results for an elasticity-based model," *Proc. Royal Soc. A*, vol. 455, no. 1988, pp. 3085–3106, Aug. 1999.

**Hua Xiong** Photograph and biography not available at the time of publication.



**Zhiheng Huang** (M'12) received the B.Eng. degree in materials engineering from Harbin Institute of Technology, Harbin, China in 2000, the M.Eng. degree in materials science from Harbin Institute of Technology, Harbin, China in 2002, and the Ph.D. degree in manufacturing engineering from Loughborough University, Loughborough, UK, in 2005. From 2006 to 2008, he was a Post Doctoral Research Associate at Loughborough University, Loughborough, UK. From 2007 to 2008, he was a Project Scientist at the Max Planck Institute for Iron Research (MPIE), Düsseldorf, Germany, on an unpaid special leave from Loughborough University. In June 2008, he returned to China and joined Sun Yat-sen University, Guangzhou, China. He is currently an Associate Professor of Materials Physics at Sun Yat-sen University. His research has been concerned with integrated computational materials engineering for semiconductor packaging and integration.



**Paul Conway** (SM'05) is the Professor of Manufacturing Processes and Associate dean for Enterprise at the Wolfsen School of Mechanical and Manufacturing Engineering at Loughborough University, where he leads the Interconnection Research Group. He is also the Director of the EPSRCs Innovative electronics Manufacturing Research Centre ([www.iemrc.org](http://www.iemrc.org)) and the recently launched EPSRC Centre for Doctoral Training in Embedded Intelligence ([www.cdt-ei.org](http://www.cdt-ei.org)). He has previously worked for Fisher Body Overseas Corporation, GMC and as an National Physical Laboratory funded research engineer at Loughborough. He has been active in contract research, training and consultancy in electronics manufacture and packaging since 1990, holding substantive research awards from the UK's EPSRC, DTI, and TSB and from the European Commission and has published widely in this field. His interests lie in: manufacturing processes; simulation; sensing, actuation and control; understanding of process-materials interactions; manufacturing knowledge management and utilisation, remanufacturing of high value assets and products, wireless sensor networks and embedded intelligent systems.